Non-linear waveform analysis for water-layer response and its application to high-frequency receiver function analysis using OBS array

Takeshi Akuhara, Kimihiro Mochizuki, Hitoshi Kawakatsu and Nozomu Takeuchi

Earthquake Research Institute, University of Tokyo, 1-1-1 *Yayoi, Bunkyo-ku, Tokyo* 113-0032, *Japan. E-mail: akuhara@eri.u-tokyo.ac.jp*

SUMMARY
Determination of a response of the sea water column to teleseismic plane wave is important to suppress adverse effects of water reverberations in calculating receiver functions (RFs) using ocean-bottom seismometer (OBS) records. We present a novel non-linear waveform analysis method using the simulated annealing algorithm to determine such a water-layer response recorded by an OBS array. We then demonstrate its usefulness for the RF estimation through its application to synthetic and observed data. Synthetic experiments suggest that the water-layer response constrained in this way has a potential to improve RFs of OBS records drastically even in the high-frequency range (to 4 Hz). By applying it to data observed by the OBS array around the Kii Peninsula, southwestern Japan, we identified a low-velocity zone at the top of the subducting Philippine Sea plate. This zone may represent the incoming fluid-rich sediment layer that has been reported by active-source seismic survey.

Key words: Body waves; Computational seismology; Subduction zone processes.

1 INTRODUCTION

Scattered teleseismic phases, such as *P*-to-*S* conversion phases, have illuminated the Earth's interior because of their high sensitivity to seismic velocity discontinuities. Conventionally, such phases are extracted from teleseismic seismograms by deconvolving the radial or transverse component with the vertical-component record (Langston 1979). The resultant time-series are termed receiver functions (RFs). The RFs provide useful approximations of the Earth's impulse response.

Recent progress in passive seismic monitoring at offshore regions has offered more opportunities to conduct RF analysis using data of ocean-bottom seismometers (OBSs; e.g. Kawakatsu *et al.* 2009; Kumar *et al.* 2011; Akuhara & Mochizuki 2015; Audet 2016 and references therein). The application of RF analysis to OBS data, however, is not straightforward, especially in the high-frequency range where the ocean water layer yields strong reverberations dominating vertical-component records. Such reverberations violate the fundamental assumption of the RF analysis that the source wavelets can be approximated by vertical-component records.

Akuhara & Mochizuki (2015) developed a method to suppress the effect of the water reverberations, utilizing a linear filter that expresses the impulse response of the water layer, namely the water-layer filter (WLF). The inverse of WLF (IWLF) is used to eliminate the multiples. The WLF was formulated by assuming vertical incidence of seismic waveforms, requiring only two tuning parameters to fully describe the filter shape: a *P*-to-*P* reflection coefficient at

the seafloor, *R*, and a two-way traveltime within the water layer, τ. Akuhara & Mochizuki (2015) determined these parameters by first estimating the source wavelet from on-land seismic station array data and then by deconvolving OBS vertical components with the source wavelet. Such an on-land array is, however, not always available at close distance from an OBS network.

This study aims to improve the WLF method to be more accessible and to demonstrate its usefulness. For this purpose, we first propose an alternative method to derive water-layer responses using only OBS data. We conduct non-linear waveform analysis to determine source wavelets and water-layer response simultaneously employing the simulated annealing (SA) method. We then show how the WLF method improves RFs using both synthetic and real observed data in a high-frequency range (up to 4 Hz).

2 NON-LINEAR WAVEFORM ANALYSIS FOR WATER-LAYER RESPONSE

Let us consider a teleseismic *P* wave recorded at a densely deployed array of OBS stations. The synthetic vertical-component records of the *i*th OBS, $u_{\mathrm{syn}}^{(i)}(t)$, may be expressed as the convolution of a source wavelet term including effects from near-source structure, $s(t)$, an impulse response of near-receiver structure, $G^{(i)}(t)$ and a time-shift to the *P*-wave arrival time, $\delta(t - t_p^{(i)})$, as follows:

$$u_{\mathrm{syn}}^{(i)}(t) = s(t) * G^{(i)}(t) * \delta\left(t - t_p^{(i)}\right), \tag{1}$$
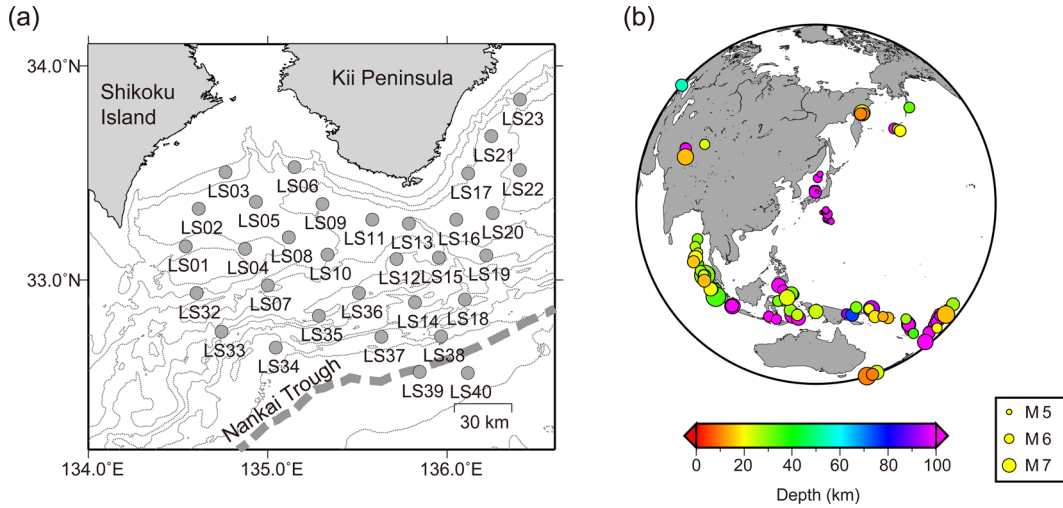
Figure 1. (a) Sites of ocean-bottom seismometers (OBSs) used in this study. Grey circles represent OBS sites. Thin lines show the water depth with the depth interval of 500 m. (b) Teleseismic and deep local events used in the inversion analysis.

where asterisk denotes convolution and $\delta(t)$ is a delta function. We recast eq. (1) by replacing the receiver term, $G^{(i)}(t)$, with WLF, $w^{(i)}(t)$, assuming a homogeneous half-space structure beneath the station with only a water layer:

$$u_{\text{syn}}^{(i)}(t) = s(t) * w^{(i)}\left(t; \tau^{(i)}, R^{(i)}\right) * \delta\left(t - t_p^{(i)}\right), \qquad (2)$$

and

$$w^{(i)}\left(t; \tau^{(i)}, R^{(i)}\right)$$
$$= \left(1 + R^{(i)}\right)\delta(t) - \sum_{n=1}^{\infty}(-1)^n\left(1 - R^{(i)n}\right)\delta\left(t - n\tau^{(i)}\right), \qquad (3)$$

where $\tau^{(i)}$ and $R^{(i)}$ are the two-way traveltime within the water layer and the reflection coefficient on the seafloor, respectively (e.g. Backus 1959; Akuhara & Mochizuki 2015).

Our inversion problem aims to determine optimum parameter sets, $\tau^{(i)}$, $R^{(i)}$, $s(t)$ and $t_p^{(i)}$, to explain observed seismograms of the entire array. For this purpose, we minimize the misfit function, E, measured as the L1 norm difference summed over multiple OBS records:

$$E = \sum_i \int \left| u_{\text{syn}}^{(i)}(t) - u_{\text{obs}}^{(i)}(t) \right| dt, \qquad (4)$$

where $u_{\text{obs}}^{(i)}(t)$ means observed vertical-component record at the *i*th OBS.

We employ the SA algorithm (Kirkpatrick *et al*. 1983) to address this high-dimensional non-linear inverse problem. We perform a random walk with a constant step interval (1 per cent of the maximum amplitude of observed waveforms) to generate trial model parameters for source wavelets, while the other parameters are generated via random samplings within a certain continuous ranges, following previous studies (Chevrot 2002; Iritani *et al*. 2010, 2014; Tonegawa *et al*. 2013). We use the same tuning parameter as Iritani *et al*. (2010) through which the SA algorithm controls probability to accept trial parameters. The final results are obtained after 2000 random generations of each model parameter. Repeating this inversion eight times using different random seeds yield no significant change (Fig. S1, Supporting Information), suggesting that our inversion results most likely converge to the global minimum rather

than local minimum. In the following result section, we show the averaged τ and R values over these eight estimates.

3 APPLICATION OF NON-LINEAR WAVEFORM ANALYSIS FOR OBS ARRAY DATA

We use data from the OBS array that was deployed around the Kii Peninsula from 2003 to 2007 (Fig. 1a). The array consists of OBSs with velocity sensors characterized by a flat frequency response above 1.0 Hz. The observation periods were different among observation sites, while 9–27 OBSs were deployed at the same time (Mochizuki *et al*. 2010). The orientations of the horizontal-component sensors were determined from the Rayleigh wave polarization (Akuhara & Mochizuki 2015). From continuous records of these OBSs, we extract *P*-wave records of teleseismic earthquakes ($M > 6.0$) at a distance range of $30°–90°$ and local deep (>300 km) events ($M > 5.0$) at a distance range of $3°–10°$. We measure signal-to-noise ratio (SNR) on the vertical-component records while conducting automatic phase picking based on short-term average to long-term average ratio algorithm (Abt *et al*. 2010). The SNR is measured by taking 1 and 4 s long time windows before and after the phase pick, respectively. We adopt events with SNR ≥ 3.0 at eight or more OBSs for the inversion analysis to determine a water-layer response at each site. We obtained 118 events through this selection (Fig. 1b).

After solving the inversion problem, we evaluate the quality of solutions by measuring cross-correlation coefficients (CCs) between synthetic and observed waveforms at each OBS (Fig. 2a). For the following discussion, we discard results of poorly fit seismograms with CC < 0.8.

The inversion results show good reproduction of observed waveforms even if the onsets of water reverberations are contaminated by coda of the direct arrivals (Fig. 2a). This insensitivity to coda contamination can be considered one of the advantages of this non-linear waveform fitting approach using the SA algorithm (e.g. Iritani *et al*. 2010). We also find consistency between our estimations for τ values and the expected timing of the reverberations from OBS depths measured by acoustic ranging (Fig. 2b).
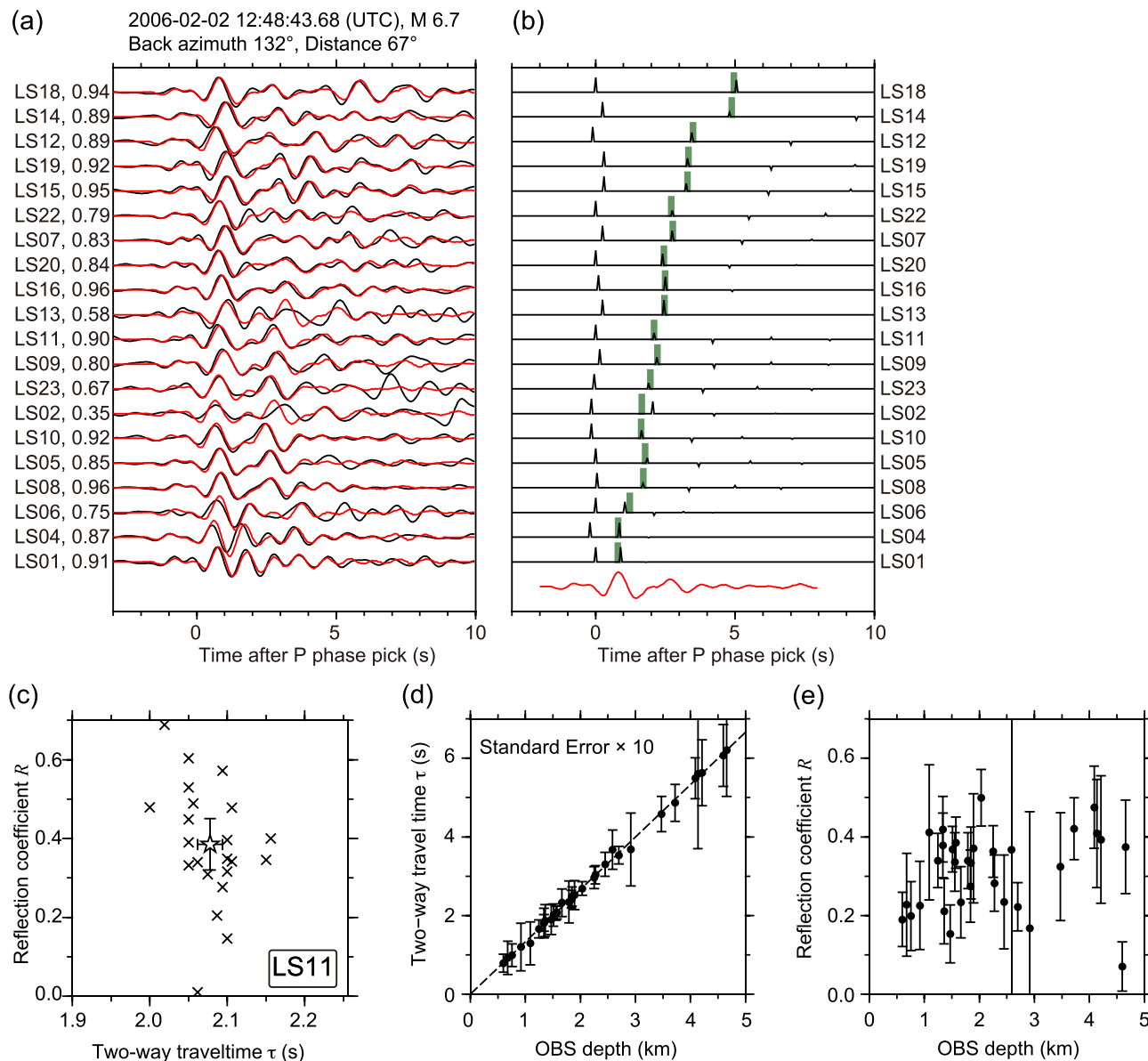
Figure 2. Results of non-linear waveform analysis. (a) Observed (black) and synthetic (red) waveforms for the event with origin time specified on top of the panel. OBS names and cross-correlation coefficients are labeled on the left side of these traces. These traces are aligned in the order of OBS depths. (b) Source wavelet (red trace) and impulse response at each OBS site (black traces) from inversion analysis. Green thick bars represent the arrival times of the first water multiples expected from the OBS depths. (c) Estimations for τ and R values from different events at a single OBS site, LS11 (crosses). The star represents their averaged values with 2σ standard errors. (d) and (e) Correlation diagram between OBS depth and averaged (d) τ and (e) R values for each OBS. Error bars denote 2σ standard errors, but are scaled by 10 for τ.

Even at the same site, individual τ and R values from different events are scattered (Fig. 2c). If this scattering comes from the dipping seafloor, there should be some correlation between individual τ (or R) values and the locations of the incident point where P wave enters into the water column. However, we do not find any apparent correlation (Fig. S2, Supporting Information). We therefore assume that the scattered τ and R distributions mainly reflect random errors in the measurements.

Examining the results from all OBSs, we can see a strong correlation between the averaged τ values and the OBS depths (Fig. 2d). The slope of this linear trend is about 0.75 km s^{-1} that is consistent with the P-wave velocity of 1.5 km s^{-1} within the water layer. Our estimations for an average R value at each OBS site show large variation from 0.1 to 0.5 (Fig. 2e). The averaged value among all

OBSs is 0.30, which is reasonable for the typical P-wave velocity and density of the marine sediment (Hamilton 1978).

4 RECEIVER FUNCTION ESTIMATION WITH INVERSE WATER-LAYER FILTER: SYNTHETIC TESTS

We calculate synthetic vertical- and radial-component records using the propagation matrix method (Haskell 1953) by assuming 1-D layered structure, composed of a water column, sediment and crust layers and a mantle half-space (Table S1, Supporting Information). In this calculation, a receiver is allowed to be placed beneath the free surface, so the effects of water reverberations are taken into
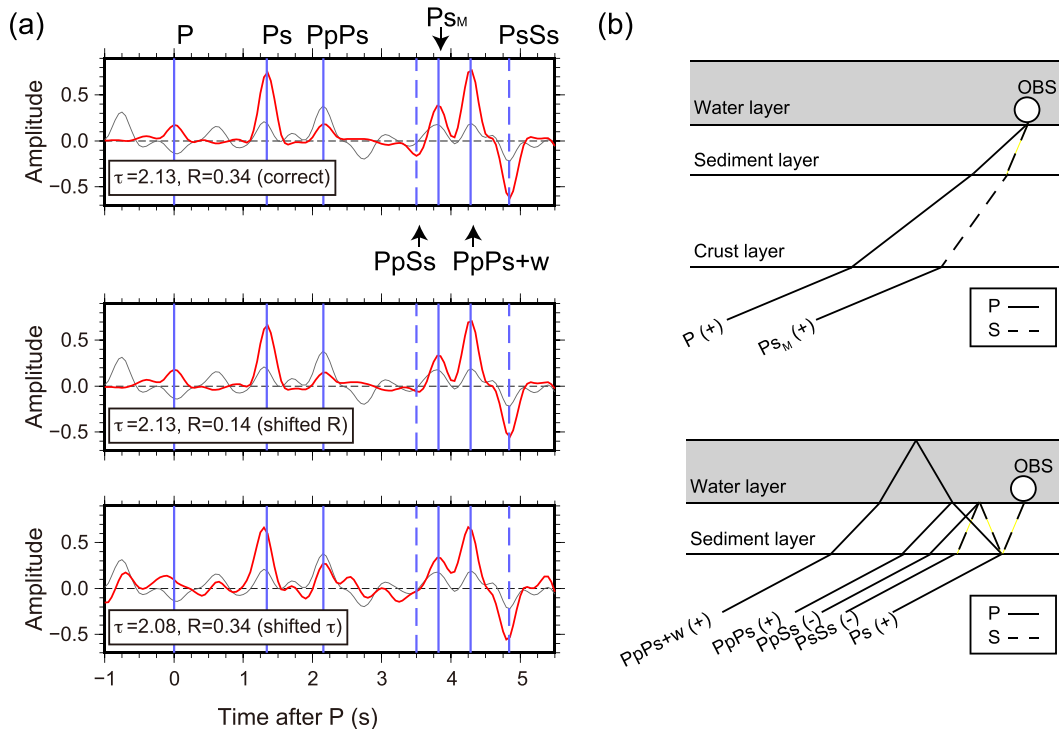
Figure 3. (a) Synthetic receiver functions (RFs). Three panels show results from different water-layer filter parameters. In each panel, red and grey traces are synthetic RFs calculated with and without the application of the inverse water-layer filter to vertical-component records, respectively. Blue solid and dashed bars represent theoretical arrival times of primary phases with positive and negative RF amplitudes, respectively. (b) Schematic illustration of primary phases which are recognizable on the synthetic tests.

consideration (e.g. Kumar *et al.* 2011). Although the formulation of the WLF (eq. 3) is based on the assumption of vertical incidence, here we employ oblique incidence with ray parameter of $0.06 \, \text{s} \, \text{km}^{-1}$ to check the validity of this assumption.

We compute two types of radial RFs by the deconvolution of the synthetic radial-component record with the synthetic vertical-component record pre-processed with IWLF and the original synthetic vertical-component record. The extended-time multitaper method (Shibutani *et al.* 2008) is incorporated through deconvolution operation. For the parameters of the IWLF, we use not only theoretical values derived from the layered model, but also slightly shifted values from the theoretical values. These shifted values aim to examine how poorly constrained parameters influence RF estimations. The resultant RFs are low-pass filtered to 4 Hz, and RFs estimated with IWLF are normalized by the factor of $1 + R$ for comparison. This amount of $1 + R$ corresponds to the energy of downward *P*-wave reflection at the seafloor which is to be removed from vertical-component records by the IWLF.

The synthetic tests show distinct advantages of the usage of the IWLF (Fig. 3a). The original RF shows many artificial peaks throughout the records which cannot be explained from the layered structure model (e.g. positive phase at 0.6 s and negative phase at 2.7 s). The RF processed with IWLF, on the other hand, shows no such artificial peaks but six isolated phases which can be interpreted as *P*-to-*S* conversion phase at the Moho (Ps_M) and the bottom of the sediment layer (Ps), and sediment-related reverberations ($PpPs$, $PpSs$, $PsSs$ and $PpPs + w$, see Fig. 3b).

We achieve the suppression of artificial peaks even when we use the shifted τ and R values. Determining the thresholds for acceptable shift amount is difficult because it depends on structure model and frequency range of low- or bandpass filter. From our experience, the

acceptable shift amounts are about ± 0.1 s and ± 0.3, for τ and R values, respectively. For most stations, the standard errors for τ and R values are below these empirical values and thus these estimation errors would not cause a severe problem in RF estimation (Figs 2d and e).

5 RECEIVER FUNCTION ESTIMATION WITH INVERSE WATER-LAYER FILTER: APPLICATION TO OBS RECORDS

We computed radial RFs for two OBSs, LS11 and LS08, using the same method as in the previous section, regarding the deconvolution operation, filtering and normalization. Teleseismic or deep local events used here are selected with the same criteria described in Section 3, but we calculate SNR for 30 s long time windows before and after the theoretical *P*-wave arrival times that are expected from the IASP91 Earth model (Kennett & Engdahl 1991). About 50 event records with SNR ≥ 3.0 on vertical components are selected for each of these two OBSs (*cf.* about 20 event records are selected in Section 3).

We can see significant differences between the RFs resulting from the two methods (Fig. 4). We conclude that the WLF method successfully improved the RF estimations based on the following three observations: (1) reduction of artificial energy before the direct *P*-wave arrivals; (2) disappearance of negative amplitudes at zero lag time at LS08, which are also considered as artificial peaks and (3) improved coherence of RFs among different events (e.g. ~1.6 s at LS08).

For both OBSs, RFs after application of IWLF indicate strong coherent peaks around ~1.5 s, although their polarities differ from
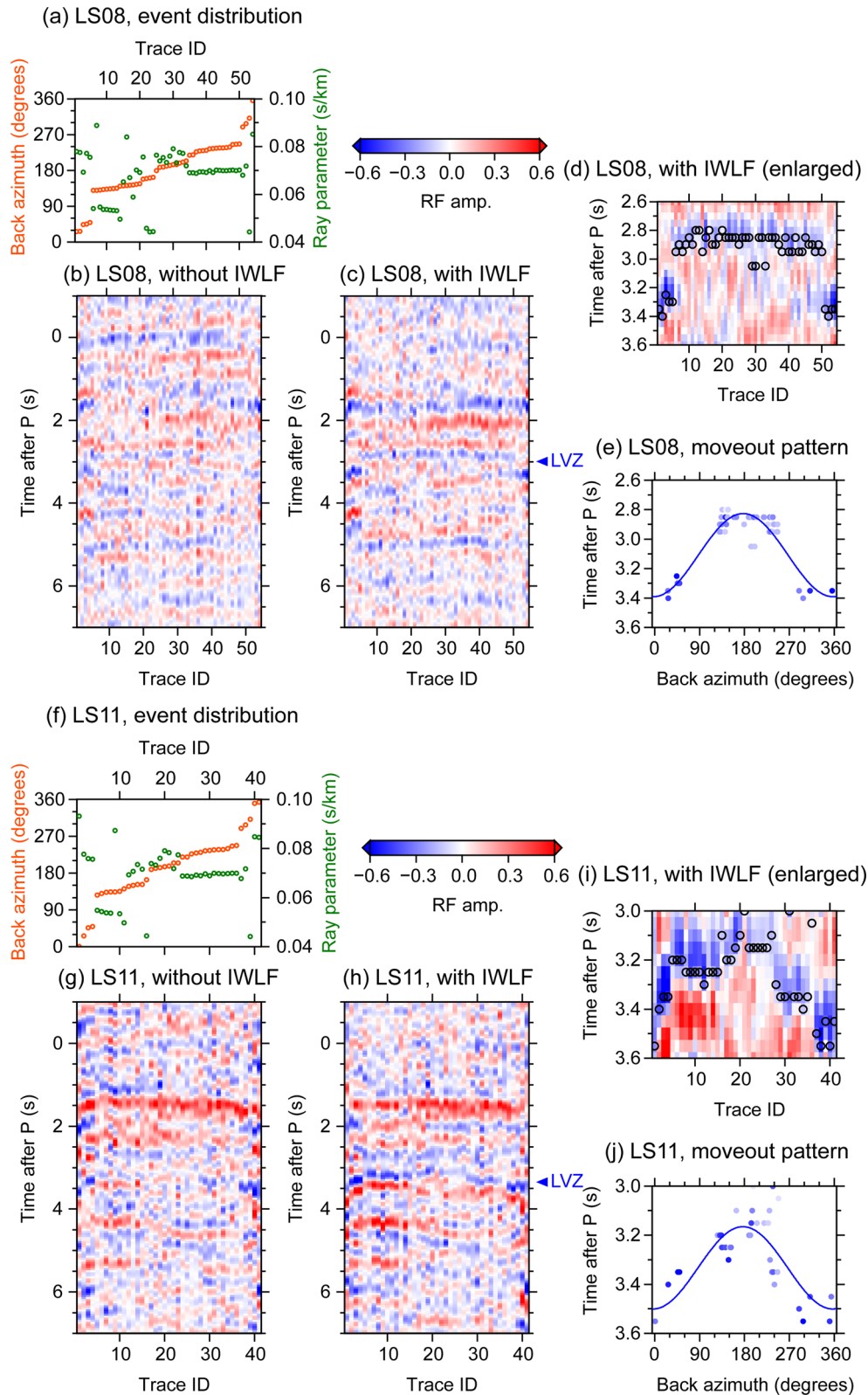
Figure 4. Radial receiver functions (RFs) calculated at two different sites, (a)–(e) LS08 and (f)–(j) LS11. (a) and (f) Backazimuth (orange circles) and ray parameter (green circles) distribution which are used to estimate RFs. (b) and (g) Radial RFs calculated without the application of IWLF to vertical-component records. (c) and (h) Radial RFs calculated with the application of IWLF. (d) and (i) Enlarged views of (c) and (h). Open circles represent the negative RF peaks. (e) and (j) Moveout pattern of the negative RF peaks along event backazimuths. Colour of each plot indicates the amplitudes of the peaks. Blue curves represent sinusoidal curve fitted to the plots.

each other. The small delay times suggest that velocity disconti-
nuities exist at very shallow depth beneath the seafloor (≤1 km
depth, if assuming typical velocity of the sediment). We interpret
the positive amplitudes at LS11 as *P*-to-*S* conversion phase from
the boundary between the unconsolidated sediment above and the
old accretionary prism below (e.g. Tsuji *et al*. 2015). In contrast, the
early negative phase at LS08 suggests the existence of inverted ve-
locity contrast. A candidate for the cause of the negative amplitude
phase is *P*-to-*S* conversion phase from a bottom simulating reflec-
tor, above which gas hydrated layer with high-velocity anomaly is
located (e.g. Harris *et al*. 2013). It is important to note that the very
shallow structure can alter the appearance of RFs drastically for the
case of OBS records.

By applying the IWLF, we recover coherent signals with neg-
ative polarities at 3.1 and 3.3 s for LS08 and LS11, respectively.
These negative signals indicate moveout patterns along event back-
azimuths characterized by a sinusoidal curve with 2π period (Figs 4e
and j). These moveout patterns of the negative peaks suggest the
existence of low-velocity zones (LVZs) with a northward dip. The
depths of these LVZs are considered to be 14 km below sea level at
LS08 and 16 km at LS11 if we assume the *P*- and *S*-wave veloci-
ties estimated by the previous 3-D tomographic analysis (Akuhara
et al. 2013). Such depths are in good agreement with the depth of
the subducting plate interface estimated by a previous study (Baba
et al. 2002). We therefore interpret that these LVZs represent the
top of the subducting Philippine Sea plate.

6 DISCUSSION

In southwestern Japan, LVZ along the plate interface has been iden-
tified by intense *P*-to-*P* reflection phases from active seismic sources
and has been interpreted as fluid-rich sediment layer (Kodaira *et al*.
2002). Although further quantitative analysis is left for future stud-
ies, the LVZ revealed by this study may also represent the same
fluid-rich layer as reported by Kodaira *et al*. (2002). Many RF stud-
ies have identified LVZs at the top of subducting plates worldwide
and have interpreted them as fluid-rich (Bostock 2013 and reference
therein). These findings have provided useful insight to better under-
stand slow slip phenomena occurring at the downdip of seismogenic
zones on megathrusts (Audet & Kim 2016 and reference therein).
In contrast, for seismogenic zones, little information has been ob-
tained by RF methods because of the limited analyses with OBS
data. Our proposed method can extend the target region seaward
and enables to access seismogenic zones.

We should note the non-uniqueness of our interpretation. As
shown in the synthetic tests, a sediment layer beneath the seafloor
causes various multiple phases on RFs, which may also be recog-
nizable in the data (e.g. ∼5.0 s in Fig. 4c). Such multiples make
interpretations of RFs difficult. Although several lines of evidence,
including the moveout patterns and the consistency with the previ-
ous plate model, support our interpretation of the LVZ at the plate
interface, more sophisticated analysis such as RF inversion analysis
would be necessary for robust interpretation.

The frequency range we used in this study (<4 Hz) is higher than
that used in ordinary RF studies (<1 Hz). Such high-frequency anal-
ysis is helpful to achieve high spatial resolution and thus the results
become more comparable with those obtained by active-source seis-
mic surveys. Most recently, detailed properties of a LVZ along the
plate interface at shallow depths has been investigated by modeling
P-to-*P* reflection waveforms of active seismic sources (e.g. Li *et
al*. 2015). Our success in high-frequency RF estimation using OBS

records provides another option to conduct such waveform model-
ing using passive seismic sources even for a wide depth range of the
plate interface. This new analysis has potential to offer additional
constraints on *S*-wave velocity or even anisotropic structure of the
plate interface at seismogenic depth. These kinds of information are
essential to discuss material and fluid content at the plate interface.

REFERENCES

Abt, D.L., Fischer, K.M., French, S.W., Ford, H.A., Yuan, H. & Romanow-
icz, B., 2010. North American lithospheric discontinuity structure im-
aged by Ps and Sp receiver functions, *J. geophys. Res.,* **115,** B09301,
doi:10.1029/2009JB006914.

Akuhara, T. & Mochizuki, K., 2015. Hydrous state of the subducting Philip-
pine Sea plate inferred from receiver function image using onshore and
offshore data, *J. geophys. Res.,* **120,** 8461–8477.

Akuhara, T. *et al.*, 2013. Segmentation of the Vp/Vs ratio and low-frequency
earthquake distribution around the fault boundary of the Tonankai and
Nankai earthquakes, *Geophys. Res. Lett.,* **40,** 1306–1310.

Audet, P., 2016. Receiver functions using OBS data: promises and limitations
from numerical modelling and examples from the Cascadia Initiative,
Geophys. J. Int., **205,** 1740–1755.

Audet, P. & Kim, Y., 2016. Teleseismic constraints on the geological envi-
ronment of deep episodic slow earthquakes in subduction zone forearcs:
a review, *Tectonophysics,* **670,** 1–15.

Baba, T., Tanioka, Y., Cummins, P.R. & Uhira, K., 2002. The slip distribution
of the 1946 Nankai earthquake estimated from tsunami inversion using a
new plate model, *Phys. Earth planet. Inter.,* **132,** 59–73.

Backus, M.M., 1959. Water reverberations—their nature and elimination,
Geophysics, **24,** 233–261.

Bostock, M.G., 2013. The Moho in subduction zones. *Tectonophysics,* **609,**
547–557.

Chevrot, S., 2002. Optimal measurement of relative and absolute delay times
by simulated annealing, *Geophys. J. Int.,* **151,** 164–171.

Hamilton, E.L., 1978. Sound velocity–density relations in sea-floor sedi-
ments and rocks, *J. acoust. Soc. Am.,* **63,** 366–377.

Harris, R., Yamano, M., Kinoshita, M., Spinelli, G., Hamamoto, H. &
Ashi, J., 2013. A synthesis of heat flow determinations and ther-
mal modeling along the Nankai Trough, Japan, *J. geophys. Res.,* **118,**
2687–2702.

Haskell, N.A., 1953. The dispersion of surface waves on multilayered media,
Bull. seism. Soc. Am., **43,** 17–34.

Iritani, R., Takeuchi, N. & Kawakatsu, H., 2010. Seismic attenuation struc-
ture of the top half of the inner core beneath the northeastern Pacific,
Geophys. Res. Lett., **37,** L19303, doi:10.1029/2010GL044053.

Iritani, R., Takeuchi, N. & Kawakatsu, H., 2014. Intricate heterogeneous
structures of the top 300 km of the Earth's inner core inferred from global
array data: I. Regional 1D attenuation and velocity profiles, *Phys. Earth
planet. Inter.,* **230,** 15–27.

Kawakatsu, H., Kumar, P., Takei, Y., Shinohara, M., Kanazawa, T.,
Araki, E. & Suyehiro, K., 2009. Seismic evidence for sharp
lithosphere-asthenosphere boundaries of oceanic plates, *Science,* **324,**
499–502.

Kennett, B.L.N. & Engdahl, E.R., 1991. Traveltimes for global earthquake
location and phase identification, *Geophys. J. Int.,* **105,** 429–465.

Kirkpatrick, S., Gelatt, C.D. & Vecchi, M.P., 1983. Optimization by simu-
lated annealing, *Science,* **220,** 671–680.

Kodaira, S. *et al.*, 2002. Structural factors controlling the rupture process of a
megathrust earthquake at the Nankai trough seismogenic zone, *Geophys.
J. Int.,* **149,** 815–835.

Kumar, P., Kawakatsu, H., Shinohara, M., Kanazawa, T., Araki, E. & Suyehiro, K., 2011. P and S receiver function analysis of seafloor borehole broadband seismic data, *J. geophys. Res.,* **116,** B12308, doi:10.1029/2011JB008506.

Langston, C.A., 1979. Structure under Mount Rainier, Washington, inferred from teleseismic body waves, *J. geophys. Res.,* **84,** 4749–4762.

Li, J., Shillington, D.J., Bécel, A., Nedimović, M.R., Webb, S.C., Saffer, D.M., Keranen, K.M. & Kuehn, H., 2015. Downdip variations in seismic reflection character: implications for fault structure and seismogenic behavior in the Alaska subduction zone, *J. geophys. Res.,* **120,** 7883–7904.

Mochizuki, K. *et al.*, 2010. Seismic characteristics around the fault segment boundary of historical great earthquakes along the Nankai Trough revealed by repeated long-term OBS observations, *Geophys. Res. Lett.,* **37,** L09304, doi:10.1029/2010GL042935.

Shibutani, T., Ueno, T. & Hirahara, K., 2008. Improvement in the extended-time multitaper receiver function estimation technique, *Bull. seism. Soc. Am.,* **98,** 812–816.

Tonegawa, T., Iritani, R. & Kawakatsu, H., 2013. Extraction of Moho-Generated phases from vertical and radial receiver functions of a seismic array, *Bull. seism. Soc. Am.,* **103,** 2011–2024.

Tsuji, T., Ashi, J., Strasser, M. & Kimura, G., 2015. Identification of the static backstop and its influence on the evolution of the accretionary prism in the Nankai Trough, *Earth planet. Sci. Lett.,* **431,** 15–25.

SUPPORTING INFORMATION

Additional Supporting Information may be found in the online version of this paper:

Figure S1. Histograms of 1σ standard deviations of (a) τ and (b) R over eight inversions using different random seeds.

Figure S2. (a) τ and (b) R values estimated from different events at a typical OBS, LS11. The size of crosses and circles show the amount of the deviations from the averaged values, and their locations represent the incident points of the first water reverberation into the sea water. Centre of each polar coordinate is identical to the OBS location, and dashed circle denotes intervals of 100 m.

Table S1. Layered structure and ray parameter used in synthetic tests.

(http://gji.oxfordjournals.org/lookup/suppl/doi:10.1093/gji/ggw253/-/DC1)

Please note: Oxford University Press is not responsible for the content or functionality of any supporting materials supplied by the authors. Any queries (other than missing material) should be directed to the corresponding author for the paper.